

A Coupled Spintronics Neuromorphic Approach for High-Performance Reservoir Computing

Nozomi Akashi,* Yasuo Kuniyoshi, Sumito Tsunegi, Tomohiro Taniguchi, Mitsuhiro Nishida, Ryo Sakurai, Yasumichi Wakao, Kenji Kawashima, and Kohei Nakajima

The rapid development in the field of artificial intelligence has increased the demand for neuromorphic computing hardware and its information-processing capability. A spintronics device is a promising candidate for neuromorphic computing hardware and can be used in extreme environments due to its high resistance to radiation. Improving the information-processing capability of neuromorphic computing is an important challenge for implementation. Herein, a novel neuromorphic computing framework using spintronics devices is proposed. This framework is called coupled spintronics reservoir (CSR) computing and exploits the high-dimensional dynamics of coupled spin-torque oscillators as a computational resource. The relationships among various bifurcations of the CSR and its information-processing capabilities through numerical experiments are analyzed and it is found that certain configurations of the CSR boost the information-processing capability of the spintronics reservoir toward or even beyond the standard level of machine learning networks. The effectiveness of our approach is demonstrated through conventional machine learning benchmarks and edge computing in real physical experiments using pneumatic artificial muscle-based wearables, which assist human operations in various environments. This study significantly advances the availability of neuromorphic computing for practical uses.

humans in a wide range of fields, such as image recognition,^[1,2] natural language processing,^[3,4] and board games.^[5,6] Despite the demand for increases in the information-processing capability of computers associated with the development of machine learning, the rate of development of conventional computers is yet to catch up with this demand.^[7] Given this background, research on neuromorphic computing devices, which are hardware that directly implements neural networks, is being actively conducted.^[8]

The magnetic tunnel junction (MTJ), which is a type of spintronics device, is a promising candidate for neuromorphic computing because of its minute size, high-speed dynamics, and high-energy efficiency.^[8–11] It has been proposed that spintronics devices can emulate major building blocks in the neural network, such as artificial synapses^[12–14] and artificial neurons,^[15] using properties that are non-volatility, plasticity, oscillatory behavior, and stochastic behavior.^[11] The application of a spin-torque oscillator (STO), which is a

limit-cycle oscillator consisting of an MTJ, to physical reservoir computing^[16–19] is an emerging research topic in which the non-linear dynamics of an STO are directly exploited as a computational resource.^[20–31] The development of a scheme to boost the

1. Introduction

Recent machine learning networks have advanced to the point where they have become comparable with or even surpassed


N. Akashi
 Graduate School of Science
 Kyoto University
 Yoshida-honmachi, Sakyo-ku, Kyoto 606-8501, Japan
 E-mail: akashi.nozomi.84z@st.kyoto-u.ac.jp

Y. Kuniyoshi, K. Kawashima, K. Nakajima
 Graduate School of Information Science and Technology
 The University of Tokyo
 Bunkyo-ku, Tokyo 113-8656, Japan

S. Tsunegi, T. Taniguchi
 Research Center for Emerging Computing Technologies
 National Institute of Advanced Industrial Science and Technology (AIST)
 Tsukuba, Ibaraki 305-8568, Japan

M. Nishida, R. Sakurai
 Digital Engineering Division
 Bridgestone Corporation
 Tokyo 104-8340, Japan

Y. Wakao
 Advanced Materials Division
 Bridgestone Corporation
 Tokyo 104-8340, Japan

 The ORCID identification number(s) for the author(s) of this article can be found under <https://doi.org/10.1002/aisy.202200123>.

© 2022 The Authors. Advanced Intelligent Systems published by Wiley-VCH GmbH. This is an open access article under the terms of the Creative Commons Attribution License, which permits use, distribution and reproduction in any medium, provided the original work is properly cited.

DOI: 10.1002/aisy.202200123

information-processing capability of spintronics devices towards the standard level of machine learning networks is an urgent and important issue to be addressed.^[21]

The MTJ has also been attracting attention as a device with significant tolerance against radiation.^[32,33] Radioactive environments, such as disaster sites, nuclear accident areas, and space, have been ongoing challenges for the areas of information sciences and engineering for many years. For example, information-processing devices have been used in a range of incidents, from the disaster at the Three Mile Island unit 2 reactor in 1979^[34,35] to the 2011 disaster at the Fukushima Daiichi Nuclear Power Plant,^[36] for various levels of use. Conventional electronic devices that implement artificial neural networks break down easily, and they do not perform normally with radiation exposure.^[37,38] A single-event effect is a radiation effect that can be characterized by a temporary change in the electronic state caused by a particle striking a sensitive node in the electronic device.^[37,38] The influence of the single-event effect is becoming increasingly serious, owing to the minimization and high integration of electronics in recent devices. Spintronics devices are robust to radiation in principle, because they use spin instead of an electric charge, unlike dynamic random access memory and flash. The tolerance of MTJs to single-event effects of different radiation types, such as heavy ion,^[39–41] neutron,^[42] proton,^[43] and gamma ray,^[42,43] has been studied.

This article proposes a novel information-processing framework based on a spintronics device that exhibits high performance and is robust in a radioactive environment (Figure 1). The proposed framework is called a coupled spintronics reservoir (CSR), in which multiple STOs are randomly connected through magnetic fields to enhance computational power for solving real-

world tasks. Through numerous numerical experiments, we show that CSRs exhibit diverse repertoires of dynamics, which can be generated only by tuning the input and coupling configurations while fixing the internal configurations of STOs, such as device size and material constants. In addition, the performance of edge computing in physical experiments is drastically improved in suitable input-coupling configurations. Consequently, CSRs outperform an echo-state network (ESN),^[17] which is a typical artificial recurrent neural network, with the same number of nodes in benchmarks and edge computing. Our results suggest that a CSR can be a powerful option for information processing in radioactive environments.

We demonstrate the effectiveness of our framework for real-world tasks through edge computing in sensors of a pneumatic artificial muscle (PAM), which is a soft actuator composed of a rubber tube and braided codes. We chose edge computing in PAM wearables as a touchstone of the CSR for the following three reasons. First, reservoir computing has been proven effective in edge-computing tasks due to its low computational cost and its ability to solve multitasking problems without learning interference. Second, although the behavior of a PAM is difficult to control because of its high dimensionality, nonlinearity, and hysteresis,^[44,45] the reservoir computing approach can solve PAM sensor emulation tasks with high accuracy.^[45–47] Finally, because of the danger of radiation for humans, assistance devices for human workers are important in radioactive environments as well as spintronics devices. Today, at disaster sites, various tasks are still handled by humans, such as rescue activities in rubble, in places where large and heavy machinery cannot enter, and other tasks in a wide range of situations. Furthermore, if a worker's job requires them to visit radioactive environments, such as exploration of the moon or Mars, assistance devices for human workers will become essential. Therefore, in this study, to demonstrate the range of validity of our approach, we use PAM sensor emulation tasks and a gait classification task for a PAM-based wearable device that assists human walking. This approach contributes to retaining the softness of the wearables, which can potentially allow for the detachment of rigid sensory devices and the implementation of robust information processing in radioactive environments. Performances of standard benchmark tasks for RNNs are presented in the Supporting Information.^[48]

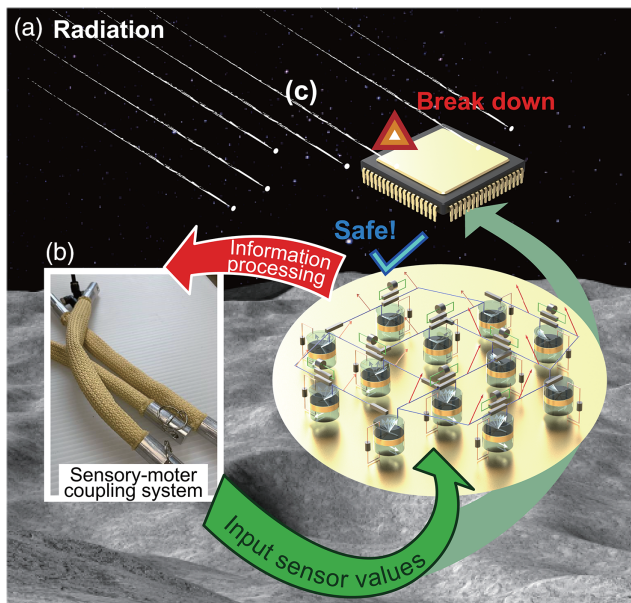


Figure 1. Schematic illustration of our framework. a) A radioactive environment. b) The sensory-motor coupling system in a radioactive environment. c) Robust information processing in a radioactive environment. The spintronics device is robust to radiation exposure, where conventional computing devices break down.

2. Results

2.1. Spin-Torque Oscillators

Let us first introduce the concept of CSRs comprising STOs. The MTJ is a spintronics device that consists of ferromagnetic metal/nonmagnetic spacer/ferromagnetic metal thin films (Figure 2a(i)). Two ferromagnets are classified as free and reference layers, where the magnetization in the former can change its direction under the application of an electric current and/or magnetic field to the trilayer, while that of the latter is fixed. By injecting an electric current into the MTJ, the transfer of spin angular momentum^[49] from conducting electrons to the free layer excites limit cycle oscillation of the magnetization. An MTJ used as a nanometer-scale auto-oscillator is called an STO. This oscillation can be detected by the tunnel magnetoresistance

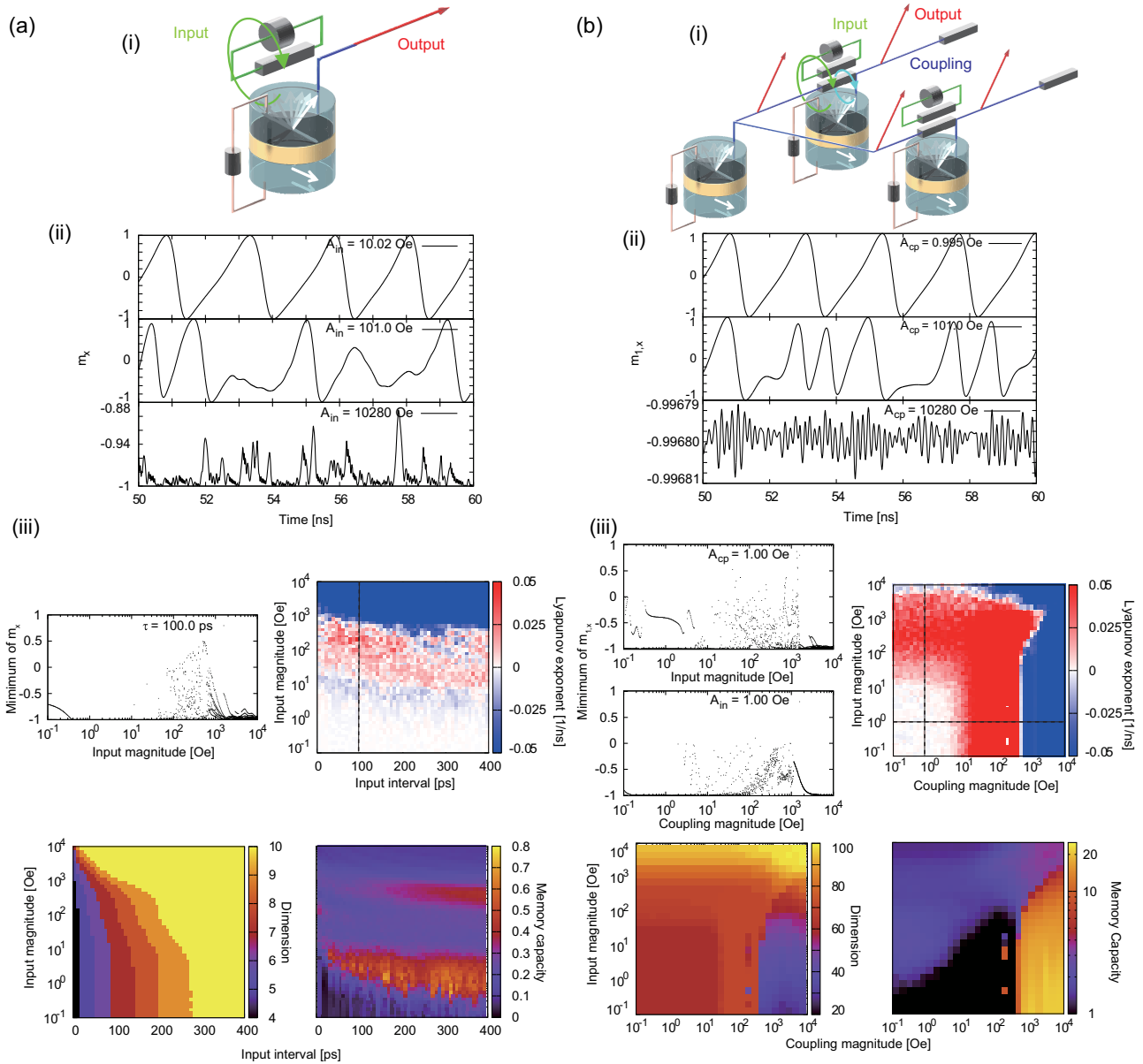


Figure 2. a) Schematics and dynamics of the single spintronics reservoir. b) Schematics and dynamics of the CSR. (i) Schematics of the spintronics reservoir. (ii) Typical time series of the x component of STO magnetization with an input interval of 100 ps. The input magnitude is set to 10.02 Oe in (b). (iii) The top-left figures are bifurcation diagrams. The top-right figures are color maps of the conditional Lyapunov exponent. The black dotted lines are the condition sets of the horizontal lines in the bifurcation diagram. The bottom-left figures are the color maps of dimension D_{rank} . The bottom-right figures are the color maps of MC[499].

(TMR) effect,^[50,51] where the output power is proportional to the vector inner products between the magnetizations in the free and reference layers. It has been recently revealed that STOs also exhibit complex dynamics, such as synchronization and chaos, by setting up feedback loops^[52,53] or inputting external signals.^[29,54–56] The proposed CSR is a new type of physical reservoir comprising multiple STOs, where we inject an input signal as a magnetic field pulse and detect the output current resulting from the TMR effect (Figure 2a(i),b(i)).

Magnetic fields are also used to realize couplings among multiple STOs, making the system high dimensional. As mentioned above, the output power from an STO is proportional to the projection of the magnetization in the free layer to that in the reference layer; therefore, it stores information pertaining to the magnetization direction. Such an output electrical power can be transformed to a magnetic field through Ampère's law. Therefore, by applying the magnetic field generated from the output power of an STO to the other STOs, as illustrated in

Figure 2b(i), the magnetization dynamics in CSR are coupled. Previously, two approaches were developed that use multiple spintronics devices as a resource for physical reservoir computing: a parallel use without coupling^[21,24] and a neighborhood interaction with dipolar fields.^[25,57,58] The proposed magnetic field coupling is less topologically restricted than neighborhood interaction coupling,^[25] as the former is performed through electrical wires. In addition, the advantage of magnetic field coupling is its high level of controllability, because it is transformed from a current. Therefore, we can easily tune coupling configurations after fixing the configurations of each STO.

Making the reservoir system high dimensional through couplings has the following three advantages. First, the CSR with appropriate configurations has higher information-processing capability than a spintronics reservoir that uses the same number of STOs in parallel due to its complex dynamics. Second, we can select the appropriate information-processing capability from repertoires of diverse dynamics depending on the target task. Finally, a multiinput setting CSR can be implemented naturally. The number of input ports in physical reservoir computing is usually limited because they are implemented as a physical device; however, the number of input ports in a CSR can be increased by connecting multiple STOs.

The dynamics of k th ($k = 1, \dots, N$) magnetizations $\mathbf{m}_k = (m_{k,x}, m_{k,y}, m_{k,z})^T \in \mathbb{R}^3$ in a CSR can be described by the Landau–Lifshitz–Gilbert (LLG) equation.

$$\frac{d\mathbf{m}_k}{dt} = -\gamma\mathbf{m}_k \times [\mathbf{H}_k + \mathbf{H}_k^{\text{cp}} + \mathbf{H}_k^{\text{in}}] - \gamma H_{s,k}\mathbf{m}_k \times (\mathbf{p} \times \mathbf{m}_k) + \alpha\mathbf{m}_k \times \frac{d\mathbf{m}_k}{dt} \quad (1)$$

$$H_{s,k} = \frac{\hbar\eta I}{2e(1 + \lambda\mathbf{m}_k \cdot \mathbf{p})MV} \quad (2)$$

The magnetic field $\mathbf{H}_k = [H_{\text{appl}} + (H_K - 4\pi M)m_{k,z}]\mathbf{e}_z$ comprises an applied field H_{appl} , interfacial magnetic anisotropy field H_K , and demagnetization field $-4\pi M$. Here, we use a Cartesian coordinate in which the z -axis is perpendicular to the film plane, while the x -axis is parallel to the magnetization \mathbf{p} in the reference layer. The output power from the STO is proportional to $\mathbf{m}_k \cdot \mathbf{p}$ because of the TMR effect mentioned earlier. The vectors \mathbf{m}_k and \mathbf{p} are normalized to be unit vectors. The saturation magnetization and volume of the free layer are denoted as M and V , respectively. The spin-transfer torque strength $H_{s,k}$ is characterized by the spin polarization η , the current I , and spin-transfer torque asymmetry λ . The magnetization \mathbf{p} in the reference layer is fixed to a positive x . The coupling magnetic field \mathbf{H}_k^{cp} and input magnetization field \mathbf{H}_k^{in} are given by the following equations.

$$\mathbf{H}_k^{\text{cp}} = A_{\text{cp}} \sum_i^N w_{k,i}^{\text{cp}} m_{i,x} \mathbf{e}_x \quad (3)$$

$$\mathbf{H}_k^{\text{in}} = A_{\text{in}} \sum_i^{N_{\text{in}}} w_{k,i}^{\text{in}} u_i(t) \mathbf{e}_x \quad (4)$$

where A_{cp} and A_{in} are the coupling magnitude and input magnitude, respectively, and \mathbf{e}_x is the x directional unit vector.

The internal coupling weight $W_{\text{cp}} = (w_{k,i}^{\text{cp}}) \in \mathbb{R}^{N \times N}$ is a matrix in which all diagonal components are 0 with no self-coupling and nondiagonal components are random variables from a uniform distribution with the interval $[-1, 1]$. The spectral radius of W_{cp} is set to 1. The input weight matrix $W_{\text{in}} = (w_{k,i}^{\text{in}}) \in \mathbb{R}^{N \times N_{\text{in}}}$ is composed of a uniform distribution with interval $[-1, 1]$, where N_{in} is the number of inputs. The input signal is expressed as $\mathbf{u}(t) = (u_1(t) \dots u_{N_{\text{in}}}(t))^T$. We do not introduce a delay term in these couplings. We numerically simulate Equation (1) using the fourth-order Runge–Kutta method. The STO parameters are set to reflect a real-world setting and are derived from a previous experiment^[59] together with a theoretical analysis^[60] (see Experimental Section for details). Furthermore, we tune the applied magnetic field H_{appl} into an experimentally reasonable range to enhance the information-processing capability of the reservoir. In the current study, we only tune the input and coupling parameters that can be easily tuned, unlike an STO's internal parameters.

The input signal $\mathbf{u}(t)$ is a discrete-point series $\mathbf{u}_n(n = 0, 1, \dots)$ that is changed in the constant input interval τ , as follows: $\mathbf{u}(t) = \mathbf{u}_n(n = \max\{n \in \mathbb{N} | n < t/\tau\})$. These piecewise constant input forms are widely used not only in spintronics reservoirs^[20–24,29] but also in other type of physical reservoir computing.^[61–65] The reservoir states of N STOs are obtained at every τ/L time, where $L \in \mathbb{N}$ is the number of time multiplexing. The above time multiplexing is used to increase the information-processing capacity by extending the virtual nodes from N to $L \times N$.^[20,22,64] Therefore, the reservoir states corresponding to the input signal \mathbf{u}_n are described by $x_n^{k,l} = m_{k,x}(n\tau + l\tau/L)$, where l ($l = 1, \dots, L$) is the time multiplexing number and k ($k = 1, \dots, N$) is the STO number. The output vector $\mathbf{y}_n = (y_{n,1} \dots y_{n,N_{\text{out}}})^T \in \mathbb{R}^{N_{\text{out}}}$ that is linearly generated from the virtual nodes vector $\mathbf{x}_n = (1, x_n^{1,1}, \dots, x_n^{N,L})^T \in \mathbb{R}^{NL+1}$, including a bias, is given as $\mathbf{y}_n = W^{\text{out}} \cdot \mathbf{x}_n$, where the output weight $W^{\text{out}} \in \mathbb{R}^{N_{\text{out}} \times (NL+1)}$ is trained by linear regression (LR) and N_{out} is the number of outputs.

2.2. Bifurcation and Memory Capacity of Spintronics Reservoirs

Here, we analyze the STO dynamics and its corresponding information-processing capability as a reservoir. STOs can show synchronization and chaos by injecting the input and incorporating coupling. In general, high-dimensional dynamical systems display complex phenomena, such as hyperchaos,^[66] chaotic itinerancy,^[67] and chimera.^[68] An STO shows chimera,^[69] suggesting that the CSR has the potential to exhibit these high-dimensional phenomena by introducing coupling.

The dynamics and information-processing capability of the system are closely related. For example, the echo-state property,^[17,70] which guarantees the reproducibility of information processing, depends on the sign of the input-conditional Lyapunov exponent in the context of the generalized synchronization of dynamical systems.^[71,72] Here, the Lyapunov exponent is a criterion of the initial-state sensitivity of the system, and a positive Lyapunov exponent usually indicates chaos for closed dynamical systems. The input-conditional Lyapunov exponent ensures that the searching space of the initial-state sensitivity

is restricted only in the reservoir space without the input space. In addition, the memory capacity (MC) of an ESN increases at the edge of chaos, which is the border of order and chaos in the parameter space.^[73] The MC evaluates the linear memory capability of the system^[74] and is bound by the rank of the covariance matrix of the reservoir states, which is simply called dimension D_{rank} .^[75] Therefore, in the current study, we analyzed the input-conditional Lyapunov exponent, dimension, and MC of a single spintronics reservoir and CSR. Definitions of MC and dimension are given in the Experimental Section. The input signal \mathbf{u}_n of these analyses is 50 000 uniformly random variables with interval $[-1, 1]$. The number of time multiplexing is $L = 10$ in all reservoirs.

Before analyzing the CSR, we must analyze the dynamics and information-processing capability of a single-spintronics reservoir where the number of STOs is $N = 1$. Figure 1a(ii) presents a time series of \mathbf{m}_x for three input magnitude conditions, where A_{in} is changed to 10.02, 101.01, and 10 280 Oe from top to bottom. When the input magnitude is 10.02 Oe, the dynamics are almost periodic, and when the input magnitude is increased to 101.0 Oe, the periodic structure collapses. When the input magnitude is further increased to 10 280 Oe, the dynamics stay in the narrow region and slightly respond to the input signal. Figure 1a(iii) (upper left plot) shows a bifurcation diagram of the single-spintronics reservoir this is determined by the input magnitude, where the minima of \mathbf{m}_x after a sufficiently long transient time are plotted. In a certain input magnitude range, where the minima are spread like points, we confirm two-step bifurcations that move from order to chaos and from chaos to order. To analyze these bifurcations quantitatively, we calculate the input-conditional Lyapunov exponents. These exponents, in accordance with the input magnitude and input interval, are plotted in Figure 2a(iii) (upper right diagram). We can confirm the existence of two bifurcations, from order to chaos and from chaos to order, at all input intervals. These two-step bifurcations also appear in the STOs where random inputs are injected as a current.^[29]

D_{rank} and the MC of a single spintronics reservoir are depicted in Figure 1a(iii) (lower-left diagram). D_{rank} is bound by $D_{\text{total}} = L = 10$ in this time multiplexing, where D_{total} is the number of reservoir states; however, when the input magnitude and input interval are small, such as $A_{\text{in}} = 10^1$ Oe and $\tau = 100$ ps, D_{rank} is less than D_{total} , and it is apparent that multiplexed virtual nodes are not fully used. D_{rank} can be used as a criterion for determining the number of time multiplexing. It has been established that the MC peaks around the edge of chaos.^[29,73] The same phenomena are found around the edge of chaos of our result when the input interval is larger than 200 ps (Figure 2a(iii), lower right diagram). However, when the input interval is less than 200 ps and D_{rank} is less than D_{total} , a peak does not always appear around the edge of chaos.

We conducted the same analysis performed on the single-spintronics reservoir for the CSR with $N = 10$ in Figure 2b. We also confirmed how the performance scales to the number of STOs (See Supporting Information^[48]). We fix the input interval $\tau = 100$ ps in the following analysis. Figure 2b(ii) presents a time series of \mathbf{m}_x for three coupling magnitude conditions, where A_{cp} is changed to 0.995, 101.01, and 10 280 Oe from top to bottom. The CSR conducts the two-step bifurcation

through not only the input magnitude but also the coupling magnitude. We confirmed the order–chaos and chaos–order bifurcations through input magnitude and coupling magnitude in a time series, bifurcation diagrams, and the color map of the input-conditional Lyapunov exponent.

The color map of the dimension indicates that the dimension fulfills $D_{\text{rank}} = D_{\text{total}} = 10 \times 10$ at certain input magnitudes and coupling magnitudes. In addition, the dimension drastically reduces at the chaos–order bifurcation point based on an increase in the coupling magnitude. The MC drastically increases rather than decreases in this region. Here, the highest MC is 21.25, even through the dimension is $\approx D_{\text{rank}} = 40 \ll 100 = D_{\text{total}}$; although the total capacity of the reservoir is small, a large proportion of the capacity occupies a linear capacity. This highest MC is larger than 10 times the highest value of the single spintronics reservoir ($8.0 = 0.8 \times 10$), which means the theoretical highest MC of the parallel spintronics reservoir with the same number of STOs.

2.3. PAM and Wearable Devices

Here, we examine a McKibben-type PAM, as shown in Figure 3a, as a soft actuator for wearable devices.^[44,76–80] Wearable devices should be lightweight to safely provide the wearer with soft movement or reduce the burden on the wearer. McKibben-type PAMs are formed of flexible polymeric materials, and because of the flexibility and lightness of the materials themselves, they have the following characteristics: 1) High force-to-weight ratio compared with conventional cylinders and electric motors. 2) High durability against impact and vibration because of their flexible constituent materials. 3) Novel types of flexible actuators leading to the possibility of new applications.

Therefore, McKibben-type PAMs are promising components for use in wearable devices and for realizing soft motion. In addition, there is no need for electronics at the actuation site and no risk of malfunction under the radiation tolerance described earlier. Simultaneously, the effect of radiation on the mechanical properties of rubbers, which are materials used in PAMs, is relatively smaller than that of other soft materials.^[81,82]

Figure 3b–d shows the relationships between contraction force and the contraction rate of the PAM, our wearable device, and the measuring system of the PAM, respectively. When the inside of the tube is pressurized, the PAM shrinks axially while expanding radially. The dynamics of the rubber itself, specifically the nonlinearity of the friction between the rubber and fiber, exhibit hysteresis in the shrinkage characteristics. In our wearable device, PAMs are used as actuators and simultaneously as sensors for controlling walking assistance. The configurations of the PAMs in our wearable device are presented in Experimental Section 4.4. The wearer walks with support equipment: a holding supporter and shoes in which artificial rubber muscles are attached; the equipment is light, and the burden is small.^[77] As indicated in Figure 3c, the PAM is placed in the calf and thigh areas. The electric resistance of the PAM is measured with a resistance meter, and the applied pressure is measured with a pressure gauge (Figure 3d).

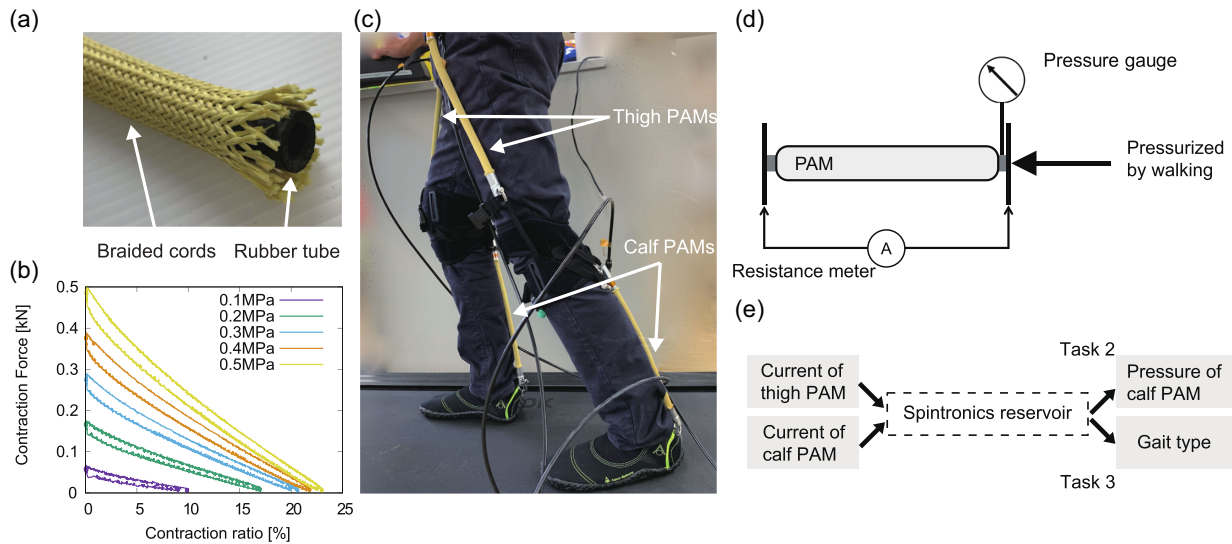


Figure 3. PAM as a component of our wearable device, its sensing scheme, and the tasks. a) A picture of the McKibben PAM used in this study. b) Contraction force and hysteresis under isobaric conditions. c) A picture of the wearable device used in this study. d) Schematic showing the measuring system of PAM. e) Schematic of input/output relation in machine learning tasks used in this study.

2.4. Tasks and Setting

The following three PAM tasks are solved using the CSR. 1) A single PAM length sensor emulation task. Predicting PAM length values from random actuating pressure values. 2) A pressure sensor emulation task in the wearable device. Predicting PAM pressure values from resistance values during walking. 3) Gait and velocity classification tasks. Classifying the gait (walk or run) and velocity (1, 3, 5, 7, or 9 mph) individually or simultaneously from the resistance values.

In the following analysis, the number of nodes of ESNs is fixed as $D_{\text{total}} = 100$, and the CSR has $N = 10$ and $L = 10$. Here, A_{in} and A_{cp} of the ESNs and CSRs are optimized by the grid search for each task. We compare their performances with the ESN with the same number of nodes as the CSRs. Detailed formulations of the ESNs are given in Experimental Section.

The single PAM length sensor emulation task is a preliminary task for edge computing of the wearable device. In task 1, we predict the length sensor value of the single PAM from the pressure value under random pressurized conditions. This task demands memory and nonlinear information-processing capability and can be effectively solved by ESNs.^[45] The PAM used in the PAM length emulation task is not attached to the wearable device, but the sampling and actuating interval is $\tau = 0.1$ s, which is the same as the sampling interval of the wearable device considered in the following tasks. The load values added to the PAM include three conditions: 100, 200, and 300 N. In task 2 and 3 of the wearable devices, the load value is variable depending on human walking. In the tasks, we use 50 000 data points, which include 1,000 washout data points, 40 000 training data points, and 9,000 evaluation data points. We use the following normalized mean squared error (NMSE) as a measure to evaluate the task performance.

$$\text{NMSE} = \frac{\frac{1}{K} \sum_{i=1}^K (\tilde{y}_i - y_i)^2}{\sigma^2(\tilde{y}_i)} \quad (5)$$

where K is the number of evaluation data points, y_i is the prediction signal, \tilde{y}_i is the target signal, and $\sigma^2(\tilde{y}_i)$ is the variance of \tilde{y}_i .

In task 2, we emulate the pressure sensor attached to the PAM on the calf from the electric resistances of the thigh and calf so that we can remove the sensory device, which is often rigid, from the platform and keep the platform flexible and soft. In addition, Kanno et al.^[77] developed a wearable device by adapting McKibben-type PAMs; here, the timing of the assistance is estimated from the pressure change of the PAM worn on the inflatable shank, and the walking motion is assisted by applying pressure to the PAM at suitable time intervals. Therefore, task 2 not only involves emulating the pressure sensor and potentially detaching it from the wearable device but also testing whether the current scheme can be exploited to detect the timing of the assistance.

In task 3, we predict the wearer's gait state based on the electric resistance value of the PAM. We can also use assistance schemes, depending on the gait type, using this information. This information will help in realizing robust assistance controls. Through these tasks, we investigate the potential to simplify the equipment itself by excluding the pressure sensor and peripheral equipment while providing more robust assistance control.

We conducted walking experiments, as presented in **Table 1**. We measured resistances and pressures using just a single leg. Using both thigh and calf PAMs, the resistance and pressure values were measured from each PAM, which yielded 1,600 temporal data points for each gait type. The data were collected at a 10 Hz sampling rate. The input–output relationship of the tasks is summarized in Figure 3e. The two input signals, which were used for both tasks 2 and 3, were the thigh- and calf-normalized

Table 1. Experiment data on the wearable device.

Name	Velocity [mile hour ⁻¹]	Gait type	Assist
<i>a</i>	1	walk	no
<i>b,h</i>	3	walk	no and yes
<i>c</i>	5	walk	no
<i>d</i>	5	run	no
<i>e</i>	7	walk	no
<i>f,i</i>	7	run	no and yes
<i>g</i>	9	run	no

currents. The preprocessing of the PAM time series is presented in Experimental Section 4.5. In task 2, we conducted the analysis from *a* to *g*, which are points without assistance control provided by the wearable device, as shown in Table 1. In task 3, we conducted the analysis from not only *a* to *g* but also *h* and *i*, which are points with walking assistance provided by the wearable device, as shown in Table 1.

2.5. Task 1: Single PAM Length Sensor Emulation

The results of task 1 are presented in Figure 3 and Table 2. A color map of a single PAM length sensor emulation performance, in terms of an NMSE with a load of 200 N, is shown in Figure 4a. The performances are drastically improved in the second bifurcation when increasing the coupling magnitude,

Table 2. NMSEs of single PAM length sensor emulation.

Task ^{a)}	Reservoir type	
	ESN $D_{\text{total}} = 100$ ($A_{\text{cp}}, A_{\text{in}}$)	CSR $D_{\text{total}} = 100$ ($A_{\text{cp}}, A_{\text{in}}$)
PAM 100 N	0.079 (0.5, 1)	0.069 (9192, 3740)
PAM 200 N	0.081 (0.4, 1)	0.051 (9192, 5910)
PAM 300 N	0.137 (0.5, 1)	0.116 (9192, 5910)

^{a)}The numbers in bold represent the best performance in each line.

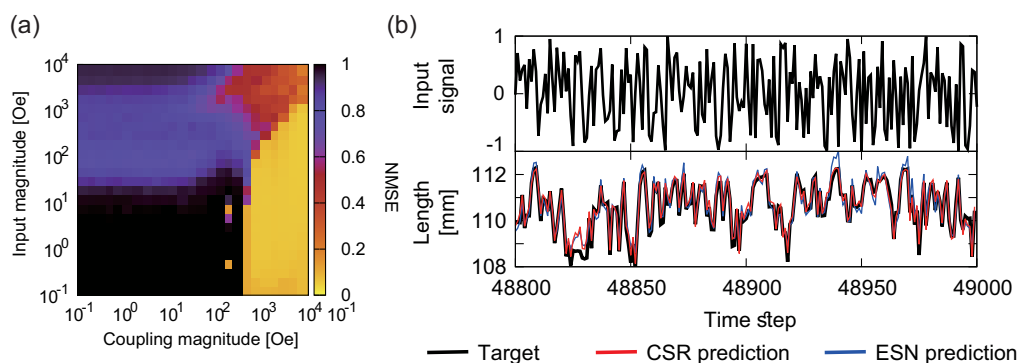


Figure 4. Results of the single PAM length sensor emulation task under a load of 200 N. a) The color map of the NMSE. b) Target and prediction time series of the best configuration of coupling and input magnitude.

which is similar to the behavior of the MC shown in Figure 2b(iii), but there are minor differences here. The ordered dynamics with a high coupling magnitude can process input signals well and not only linearly but also nonlinearly, while almost the entire capacity is spent linearly, as shown in the dimensions of Figure 2b(iii). Table 2 shows that the best CSRs outperform the ESNs in all load conditions. Figure 4b illustrates the prediction signals of the best performance in Table 2. We can visually confirm that a CSR exhibits better prediction power than ESN. These results indicate that a CSR effectively processes not only linear information but also nonlinear information, such as the PAM nonlinear dynamics.

2.6. Task 2: Wearable Pressure Sensor Emulation

We can solve the wearable device pressure sensor emulation task using the CSR. The schematics of the task are presented in Figure 5a. The calf pressure value is predicted from the normalized current values of the thigh and calf PAMs in this task. Because the calf pressure value can be used for detecting a walking state, such as a preswing phase, it is used for determining the assistance timing.^[77] Furthermore, we conducted multitasking that predicted not only the current pressure value but also *s* second future pressure values, where *s* is the prediction time, from current normalized currents. Predicting future values is practically important because the air pressure of the PAM has a large control delay and the prediction of these values can improve the control performance.^[83] Two input signals were transformed into the corresponding output time series through the reservoir. Although each STO has the same configuration, a difference between the input and coupling conditions creates diversity in the reservoir dynamics. By applying LR to these output signals from the reservoir dynamics, the outline of the pressure from current to 20 s later can be well predicted.

Table 3 presents the NMSEs of this task with prediction time $s = 0$ by LR, extreme learning machine (ELM),^[84] ESN, and CSR. LR is a model with the input signals directly combined linearly, and ELM is the ESN with $A_{\text{cp}} = 0$ (detailed formulations are given in the Experimental Section). Performances are good in the order of ESN, ELM, and LR in all gait types. Therefore, memory and nonlinearity are required for this task. In addition, the CSRs outperform the ESNs with the same number of nodes;

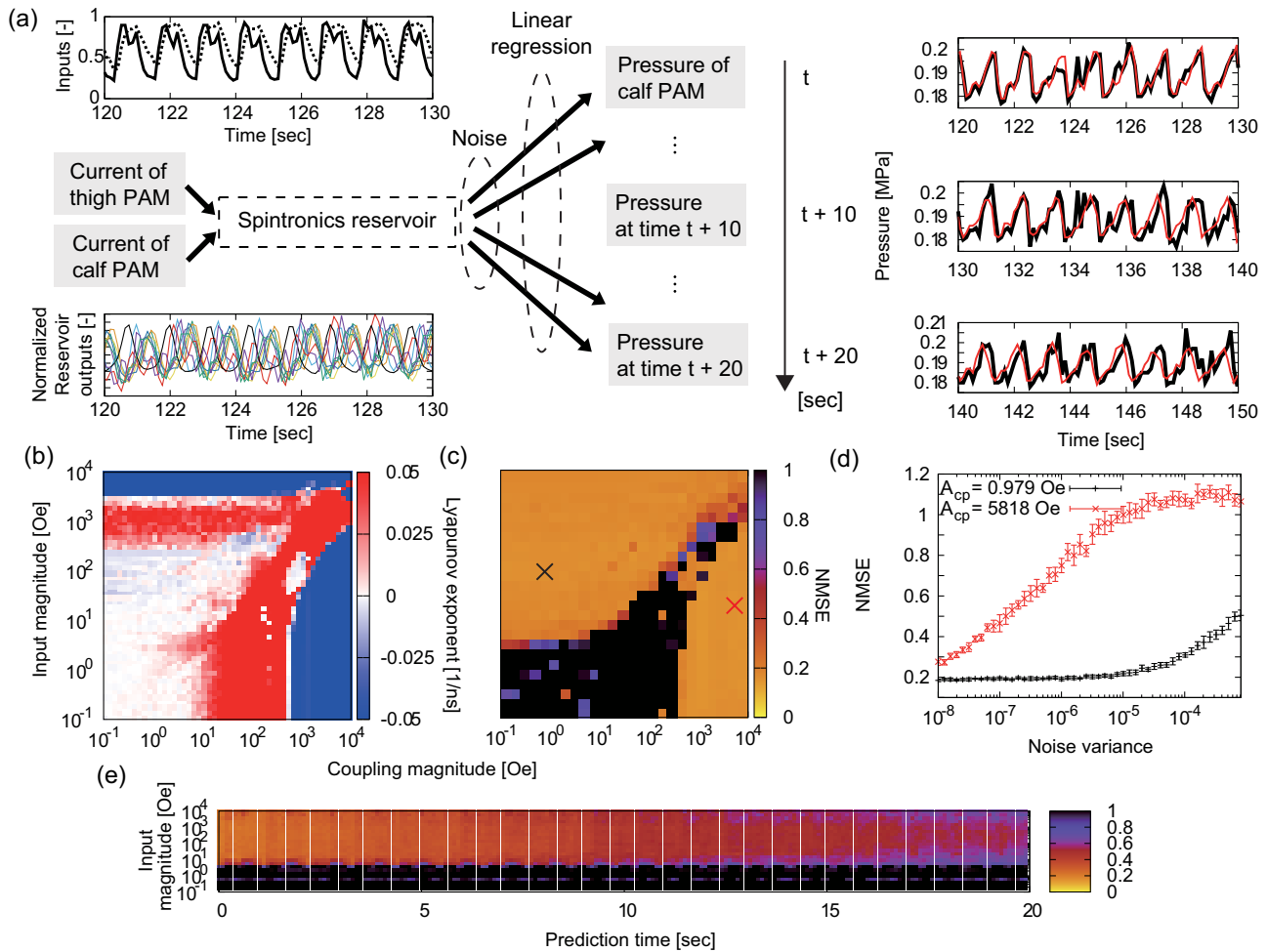


Figure 5. Wearable pressure sensor emulation tasks for a 3 mph walk. a) Schematics of the task. The top-left time series are input signals. The solid and dotted lines are the normalized currents of the calf and thigh PAMs, respectively. The bottom-left time series are the reservoir outputs. The time multiplexing virtual nodes are not plotted. The coupling magnitude and input magnitude are $(A_{cp}, A_{in}) = (1475 \text{ Oe}, 37.98 \text{ Oe})$. The time series on the right are the target signals and predicted signals for each prediction time. The black and red lines are the target and predicted signals, respectively. b) A color map of the Lyapunov exponent analyzed in each coupling and input magnitude. c) A color map of the NMSE for each coupling and input magnitude. The black and red cross marks correspond to the configuration in (d). d) Noise variance versus NMSE. The black line represents $(A_{cp}, A_{in}) = (0.979 \text{ Oe}, 94.81 \text{ Oe})$, and the red line represents $(A_{cp}, A_{in}) = (5818 \text{ Oe}, 0.963 \text{ Oe})$. The value is the mean of 20 trials, and the error bar shows the standard deviation. e) A color map of NMSE for prediction time and input magnitude. The coupling magnitude is $A_{cp} = 1475 \text{ Oe}$.

Table 3. NMSEs of the current pressure emulation of a wearable device.

Gait type ^{a)}	Reservoir type			
	LR	ELM $D_{total} = 100$ (A_{cp}, A_{in})	ESN $D_{total} = 100$ (A_{cp}, A_{in})	CSR $D_{total} = 100$ (A_{cp}, A_{in})
1 mile walk	0.244	0.249 (0, 0.1)	0.244 (0.4, 1)	0.225 (6.095, 149.8)
3 mile walk	0.206	0.179 (0, 1)	0.159 (0.2, 1)	0.146 (1475, 37.98)
5 mile walk	0.390	0.301 (0, 0.1)	0.233 (0.6, 1)	0.225 (1475, 1.546)
5 mile run	0.683	0.648 (0, 1)	0.414 (1, 0.1)	0.374 (236.7, 236.7)
7 mile walk	0.633	0.434 (0, 1)	0.328 (1.1, 1)	0.327 (0.979, 590.9)
7 mile run	0.687	0.647 (0, 0.1)	0.538 (0.6, 0.1)	0.500 (1475, 0.393)
9 mile run	0.684	0.588 (0, 1)	0.424 (1.2, 10)	0.417 (5818, 236.7)

^{a)}The numbers in bold represent the best performance in each line.

therefore, the CSRs solve the tasks more efficiently than the ESNs. Furthermore, we conducted this task with a limited sensory input using either the calf or thigh currents in the 3-mile walk experiment. The best NMSEs are 0.160 and 0.164 with only calf current input and just thigh current input, respectively. The differences in task performance between the case of multiple inputs and that of a single input are relatively small. Therefore, we can eliminate the calf sensor because the pressure of the calf PAM can be emulated by only the current of the thigh PAM through body coupling.

Figure 5b depicts a color map of the input-conditional Lyapunov exponent. The ordered dynamics region with a relatively lower-coupling magnitude performs similarly a region, showing a higher-coupling magnitude, unlike the MC result shown in Figure 2b(iii). Moreover, in the lower-coupling-

magnitude region, the performance does not decrease, despite the chaoticity of the reservoir dynamics. Further analyses into the relationships between the dynamics and information processing capability of the reservoir are required to understand this phenomenon.

Next, we analyze the noise tolerance of this task. Here, observational noise (Gaussian white noise) was added to the reservoir output signals. The input time series, which are wearable sensor values, include experimental noises. Input noises can potentially affect reservoir performance in a more complex way than observational noise. This is because of the input-induced bifurcations demonstrated in Section 2.2. Although wearable experiments focus on analyzing the dependence of the performance on observational noise, the effect of input noise is also important to remember in practical applications. Figure 5d illustrates the change in NMSE through noise variance, including the NMSE average and standard deviation of 10 different noises for each noise variance. The performance monotonically decreases for noise variance, and we confirmed that the CSR exhibits robustness against observational noise. The variance in the observational noise in the experimental device is usually $\approx 10^{-4}$. The noise tolerance of the lower-coupling-magnitude region is much better than that of the higher-coupling-magnitude region, while these regions show a similar level of task performance without noise. The dynamics of a higher-coupling magnitude are more sensitive to noise because they remain within the narrow region, as confirmed in Figure 2b(ii). Finally, we can confirm the dependency of the prediction time s on task performance. Figure 5e presents a color map of NMSE through the prediction time and input magnitude. In a certain input magnitude region, the performance has almost no deterioration until $s < 10$ s, and deterioration can be further suppressed by tuning the input magnitude.

Table 4. Accuracy of wearable device gait classification.

Classification ^{a)}	Reservoir type			
	LR	ELM $D_{\text{total}} = 100$ ($A_{\text{cp}}, A_{\text{in}}$)	ESN $D_{\text{total}} = 100$ ($A_{\text{cp}}, A_{\text{in}}$)	CSR $D_{\text{total}} = 100$ ($A_{\text{cp}}, A_{\text{in}}$)
Gait	0.687	0.806 (0, 10)	0.928 (1.2, 1)	0.935 (0.620, 37.98)
Velocity	0.271	0.381 (0, 10)	0.499 (1.2, 10)	0.499 (590.9, 590.9)
Gait and velocity	0.161	0.350 (0, 10)	0.482 (1.2, 10)	0.518 (60.01, 37.98)

^{a)}The numbers in bold represent the best performance in each line.

2.7. Task 3: Wearable Gait and Velocity Classification

We solved the wearable device gait and velocity classification tasks using the CSR. Seven types of normalized currents in the thigh and calf PAMs, as shown in Figure 6a, were prepared as the input signals. The target signal has a gait that is a walk or run; a velocity that is 1, 3, 5, 7, or 9 mph; and a combination of the gait and velocity corresponding to an input time series. The schematics of the task are presented in Figure 6b. Logistic regression is used as a multivalue classifier. Figure 6c presents two gait types in the principal component (PC) space. The 5 mph walk and 7 mph walk overlap each other in the input signal PC space; therefore, classifying them from the input time series is difficult. The reservoir-state signals that have 100 dimensions are plotted in the PC space of the reservoir output signals. The 5 mph walk and 7 mph walk are clearly separated; thus, classifying them is easier.

Table 4 presents the accuracy rate for obtaining the correct answers in the evaluation data. The performances are good, here in the order of ESN, ELM, and LR, which is the same as in task 1;

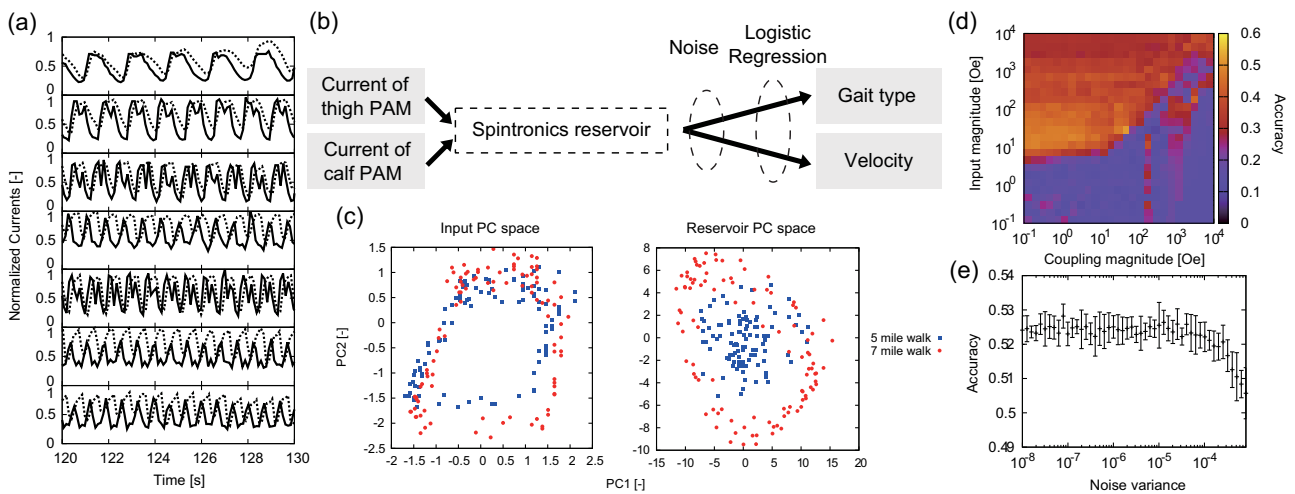


Figure 6. Wearable gait classification tasks. a) The time series on the left are input signals. The solid and dotted lines are the normalized currents of the calf and thigh PAMs, respectively. The diagrams show the cases of a 1 mile walk, 3 mile walk, 5 mile, walk, 5 mile run, 7 mile walk, 7 mile run, and 9 mile run from top to bottom. b) Schematics showing the I/O relations of the task. c) Typical examples of plots for the first- and second-principal component spaces. The left is the input signals, and the right is the reservoir-state signals. The red and blue points represent a 5-mile walk and 7-mile walk, respectively. d) A color map of the accuracy of the simultaneous classification of gait and velocity. e) Noise variance versus NMSE. ($A_{\text{cp}}, A_{\text{in}}$) = (60.01Oe, 37.98Oe). The value is the mean of 20 trials, and the error bar shows the standard deviation.

hence, memory and nonlinearity are also necessary for this task. In addition, the CSRs outperform the ESNs with the same number of nodes, suggesting that the CSRs solve the tasks more efficiently than the ESNs. The accuracy of the gait classification is over 90%, while that of the velocity classification is $\approx 50\%$, suggesting that the task is more difficult. Figure 6d shows the color map of accuracy for the input and coupling configuration of simultaneous classifications. In this task, the performance does not improve in the high-coupling-magnitude region. Figure 6e depicts the observational noise tolerance of this task. The noise is added in the same way as task 1. There is almost no deterioration until the noise variance reaches 10^{-4} , which is the same as the experimental noise variance.

In addition, we conducted the gait classification task with walking assistance provided by the wearable device. The types of gaits that we considered were a 3 mph walk and 7 mph run. As a result, the CSR solves this classification task with an accuracy of 99.8% for the best input and coupling parameters. Based on this result, a time series with walking assistance can be handled much like that without walking assistance. The details of the experimental setup and results are provided in Supporting Information.^[48]

3. Conclusion

This study proposes a high-performance neuromorphic computing scheme: a CSR. Our high-dimensional spintronics reservoir shows diverse bifurcation structures depending on the input and coupling configurations; accordingly, the information-processing capability of the spintronics reservoir drastically changes. It is difficult for a physical computing device to tune internal parameters after fixing the configurations, unlike with an artificial neural network. Therefore, a diverse repertoire obtained only from input and coupling configurations offers a great advantage as a physical computing device. We solved multiple benchmark tasks and tasks of the wearable device using the CSR. The CSR outperforms conventional neural networks in suitable task configurations, and the noise tolerance of the CSR can be improved by tuning the input and coupling configurations.

Although numerically solving the LLG equation is a promising way to comprehensively analyze magnetization dynamics, it has several limitations, such as high calculation costs and a lack of quantitative prediction.^[85] One limitation of the LLG equation-based model partially relates to the fact that experimental situations cannot be fully reproduced: the sample shape might not be perfectly circular, the concentration of atoms might not be perfectly homogeneous, and the values of several parameters, such as spin polarization and spin diffusion length, might not be known. In recent years, a prediction method using neural networks has been developed.^[85] It can reduce computational costs for the simulation of magnetization dynamics, but its limitation is that it can ignore physical constraints. Analysis methods for magnetization dynamics are still evolving. We should understand the characteristics of each approach, and it is important to choose or combine appropriate approaches for each purpose.

There are some physical limitations of the CSR configuration in the experimental implementation stage. The magnetic field,

which is used for inputs and coupling in the CSR, is generated by the electric current. The region of the large magnetic field, which was analyzed in this study, is difficult to realize using current device technology and the energy of edge computing. In addition, current-generated magnetic fields also limit the scalability of devices. STOs are physically connected to each other by electronic wire, so the scalability of the CSR is physically restricted. If we plan to use more STOs, we may consider a sparse coupling configuration or using small CSR arrays in parallel, which can weaken the restriction of scalability. In practical situations, we should choose the CSR configuration considering not only the information processing ability but also the various constraints of devices, such as the energy cost and number of couplings. However, we would like to note that we investigated difficult regions for implementation, such as a large magnetic field and fully connected nodes, to reveal the potential of the CSR. Here, the potential means the kinds of dynamics the CSR can exhibit and the kinds of applications for which it can be used in the future, such as neuromorphic supercomputers, which are not limited to edge computing.

The time scale of a real-world task for a wearable device is much larger than the time scale of the STO. The signal frequency of our wearable device is 10 Hz, while that of the STO is approximately 1 GHz. In such a situation where sensors and computers have a large difference of time scales, a method that uses a sufficient number of task signals that are stored in the external memory can be used, and these signals can be injected into the spintronics reservoir at a time to be solved. If it is used in a radioactive environment, its external memory must be constructed by a radiation-tolerant device. For example, the existing type of radiation-tolerant memory, a spintronics device as memory,^[86] or a spintronics reservoir implemented as a shift register are candidates for the external memory.

Physical reservoir computing as neuromorphic computing is implemented not only by spintronics but also other devices, such as memristors,^[87,88] atomic switches,^[89–91] photonic devices,^[62,63,92,93] and quantum devices.^[64,65,94] These devices have advantages and disadvantages, such as their dynamic speed, size, energy efficiency, and scalability. In terms of these factors, spintronics devices have the advantage of being almost commercial-level technology and the disadvantage that their scalability has not been demonstrated yet.^[8]

In the present study, we focused on the unique material property of spintronics devices that they are robust in radioactive environments. Other robust hardware, such as an atomic switch, can also be physical reservoir-computing device candidates in radioactive environments. In addition, note that this study proposes an option for a radiation resilient system for not an entire computer but a part of a computer. We can replace a conventional machine learning network with the radiation-resilient physical reservoir; however, peripheral systems, such as a measurements system and linear readout, are still not robust in radioactive environments.

Based on the results, our system is capable of implementing more practical tasks than tasks treated in this study. Although we have focused on the information-processing tasks of wearable devices, our scheme can be applied to other types of information processing, such as the communication required in a radioactive environment. Furthermore, several pretraining techniques have

been recently proposed to harness chaotic reservoirs to increase computational capability by adjusting the internal weights.^[95–97] These techniques can be introduced to the CSR in the future.

4. Experimental Section

Parameters in STOs: The values of parameters in the LLG equation were derived from an experimental study^[59] and theoretical study,^[60] as the saturation magnetization $M = 1448.3 \text{ emu.c.c}^{-1}$, interfacial magnetic anisotropy field $H_K = 18.616 \text{ kOe}$, applied field $H_{\text{appl}} = 200 \text{ Oe}$, volume of the free layer $V = \pi \times 60^2 \times 2 \text{ nm}^3$, spin polarization $\eta = 0.537$, gyromagnetic ratio $\lambda = 1.764 \times 10^7 \text{ rad}/(\text{Oes})$, spin-transfer torque asymmetry $\gamma = 1.764 \times 10^7 \text{ rad}(\text{Oes})^{-1}$, Gilbert damping constant $\alpha = 0.005$, and constant current $I = 2.5 \text{ mA}$.

ESN, ELM, and LR Systems for Comparisons: We introduced the architectures of artificial neural networks to compare them with the CSR used in this paper. First was the ESN. The i th computational node at time t was represented as x_t^i , the j th input node was represented as u_t^j , and the l th output node at time t was represented as y_t^l . The computational nodes and outputs of the ESN are given by

$$x_t^i = f \left(A_{\text{cp}} \sum_{j=1}^N w_{ij} x_{t-1}^j + A_{\text{in}} \sum_{j=1}^N w_{ij}^{\text{in}} u_t^j \right) \quad (6)$$

$$y_k^l = \sum_{i=0}^N w_{i,j}^{\text{out}} x_k^i \quad (7)$$

where the activation function was given by f , which was the hyperbolic tangent in this study; each node of the input weight $W_{\text{in}} = (w_{ij}^{\text{in}})$ comprised a uniform distribution with $[-1, 1]$, and each node of the internal weight $W = (w_{ij})$ comprised a uniform distribution with $[-1, 1]$ and was normalized because the spectral radius equaled 1. The coupling magnitude A_{cp} coincided with the spectral radius of $A_{\text{cp}}W$. The bias term x_t^0 was set as $x_t^0 = 1$. The output weight $W_{\text{out}} = (w_{ij}^{\text{out}})$ was tuned by training. In the current article, the ELM was set by eliminating the internal coupling from the ESN, so $A_{\text{cp}} = 0$ in Equation (6). The original definition of the ELM is slightly different because of the existence of the bias term. However, we selected our formulation because of its similarity to the memoryless nonlinear feed-forward neural network and its ease of comparison with the ESN. Finally, LR is given by

$$y_k = \sum_{i=1}^N w_i^{\text{out}} u_k^i + w_0^{\text{out}} \quad (8)$$

Definitions of Memory Capacity and Dimension: The memory function $m(d)$ is defined as the normalized squared correlation between the current reservoir state and past d input signal value.

$$m(d) = \frac{\langle u_{n-d} \mathbf{x}_n \rangle^T \langle \mathbf{x}_n \mathbf{x}_n^T \rangle^{-1} \langle u_{n-d} \mathbf{x}_n \rangle}{\langle u_{n-d}^2 \rangle} \quad (9)$$

where u_n is the input signal value at time n , \mathbf{x}_n is the reservoir's output vector at time n , and $\langle u_{n-d}^2 \rangle$ is the average of u_{n-d}^2 through n . (The results of the memory function of CSRs are given in the Supporting Information^[48]) In addition, $0 \leq m(d) \leq 1$ always holds. When $m(d) = 0$, the system never reconstructs past the input value u_{n-d} from the current reservoir-state vector \mathbf{x}_n , but when $m(d) = 1$, the system can completely reconstruct past the input value u_{n-d} . $\text{MC}[D]$ is defined as a sum of $m(d)$ through $d = 0, \dots, D$; therefore, we have

$$\text{MC}[D] = \sum_{d=0, \dots, D} m(d) \quad (10)$$

In addition, we defined D_{total} as the number of reservoir states and dimension D_{rank} as the number of linearly independent outputs, such that

$$D_{\text{rank}} = \text{rank}(X^T X) \quad (11)$$

where $X = (\mathbf{x}_0 \cdots \mathbf{x}_T)^T$ is the reservoir-state matrix. Here, the following important equation holds.

$$\lim_{D \rightarrow \infty} \text{MC}[D] \leq D_{\text{rank}} \leq D_{\text{total}} \quad (12)$$

In particular, if the reservoir has the echo-state property, $D_{\text{rank}} - \lim_{D \rightarrow \infty} \text{MC}[D]$ coincides with the nonlinear MC .^[75] In this study, the maximum delay D was 499 in all analyses.

Configurations of the PAM: By pressurizing the inside of the tube with fluids, the PAM shrunk axially while expanding radially. The diameter of the PAM was 11 mm and length is 250 mm. Because an ordinary diene-based rubber has low conductivity, it is difficult to measure the electrical resistance using a general electrical resistance-measuring device. Therefore, it is necessary to increase the conductivity of the PAM. In the present study, we mixed fine-particle-size carbon in the diene-based rubber and improved the conductivity from $\approx 1.0 \times 10^{-3}$ to 20 S m^{-1} .^[45]

Preprocessing of PAM Time Series: Here we described the preprocessing for PAM time series for our tasks. To wash out the STO's transient dynamics, we extended the data by duplicating the combination of 1–1,000 of the beginning data of the PAM time series. The total 2,600 data points were treated as 1,100 washout data points, 1,200 training data points, and 300 evaluation data points, respectively.

The normalized currents, which were input signals for our tasks, ensured that the reciprocals of resistances were normalized in the interval $[0, 1]$. We used the normalized current value instead of using the resistance to bring the distribution of input signals closer to uniform distribution because the distributions of the resistance value had an exponential tail.

Human Subjects: This study involved human subjects. Approval of all ethical and experimental procedures and protocols was granted by the University of Tokyo under application no. UT-IST-RE-201 125-1a. These experiments were reviewed and approved by the ethical review board of the University of Tokyo. Written informed consent was obtained from the trainees, including their consent to participate and for the findings to be published.

Supporting Information

Supporting Information is available from the Wiley Online Library or from the author.

Acknowledgements

The authors thank Mr. Shungo Fujita from the Bridgestone corporation for designing and creating figures. The results were partially obtained from a project (Innovative AI Chips and Next-Generation Computing Technology Development/(2) Development of Next-Generation Computing Technologies/Exploration of Neuromorphic Dynamics towards Future Symbiotic Society) commissioned by NEDO. K.N. was supported by JSPS KAKENHI grant numbers JP18H05472 and by JST CREST grant number JPMJCR2014.

Conflict of Interest

The authors declare no conflict of interest.

Data Availability Statement

The data that support the findings of this study are available in the supplementary material of this article.

Keywords

neuromorphic computing, physical reservoir computing, pneumatic artificial muscles, radioactive environments, spintronics

Received: May 12, 2022

Revised: August 20, 2022

Published online: September 20, 2022

- [1] K. Kowsari, M. Heidarysafa, D. E. Brown, K. J. Meimandi, L. E. Barnes, in *Proc. of the 2nd Inter. Conf. on Information System and Data Mining, ICISDM '18*, Association for Computing Machinery, New York, NY **2018**, p. 19a 28, <https://doi.org/10.1145/3206098.3206m>.
- [2] *Advances in Neural Information Processing Systems*, (Ed.: Y. Huang, Y. Cheng, A. Bapna, O. Firat, D. Chen, M. Chen, H. Lee, J. Ngiam, Q. V. Le, Y. Wu, Z. Chen, I. H. Wallach, H. Larochelle, A. Beygelzimer, F. d'Alche-Buc, E. Fox, R. Garnett), in *33rd Conference on Neural Information Processing Systems (NeurIPS 2019)*, Vol. 32, Curran Associates, Inc., Vancouver, Canada **2019**, pp. 103–112, <https://proceedings.neurips.cc/paper/2019/file/093f65e080a295f8076b1c5722a46aa2-Paper.pdf>.
- [3] J. Devlin, M.-W. Chang, K. Lee, K. Toutanova, arXiv preprint arXiv:1810.04805 **2018**.
- [4] Z. Lan, M. Chen, S. Goodman, K. Gimpel, P. Sharma, R. Soricut, in *Int. Conf. on Learning Representations*, Addis Ababa, Ethiopia **2020**, <https://openreview.net/forum?id=H1eA7AEtVS>.
- [5] D. Silver, J. Schrittwieser, K. Simonyan, I. Antonoglou, A. Huang, A. Guez, T. Hubert, L. Baker, M. Lai, A. Bolton, Y. Chen, T. Lillicrap, F. Hui, L. Sifre, G. Van den Driessche, T. Graepel, D. Hassabis, *Nature* **2017**, *550*, 354.
- [6] D. Silver, T. Hubert, J. Schrittwieser, I. Antonoglou, M. Lai, A. Guez, M. Lanctot, L. Sifre, D. K. Maran, T. Graepel, T. Lillicrap, K. Simonyan, D. Hassabis, *Science* **2018**, *362*, 1140.
- [7] N. C. Thompson, K. Greenewald, K. Lee, G. F. Manso, arXiv preprint arXiv:2007.05558 **2020**.
- [8] D. Markovic, A. Mizrahi, D. Querlioz, J. Grollier, *Nat. Rev. Phys.* **2020**, *2*, 499.
- [9] K. Kudo, T. Morie, *Appl. Phys. Express* **2017**, *10*, 043001.
- [10] M. Romera, P. Talatchian, S. Tsunegi, F. Abreu Araujo, V. Cros, P. Bortolotti, J. Trastoy, K. Yakushiji, A. Fukushima, H. Kubota, S. Yuasa, M. Ernoult, D. Vodenicarevic, T. Hirtzlin, N. Locatelli, D. Querlioz, J. Grollier, *Nature* **2018**, *563*, 230.
- [11] J. Grollier, D. Querlioz, K. Camsari, K. Everschor-Sitte, S. Fukami, M. D. Stiles, *Nat. Electronics* **2020**, *3*, 360.
- [12] Y. Cao, A. Rushforth, Y. Sheng, H. Zheng, K. Wang, *Adv. Funct. Mater.* **2019**, *29*, 1808104.
- [13] A. Kurenkov, S. DuttaGupta, C. Zhang, S. Fukami, Y. Horio, H. Ohno, *Adv. Mater.* **2019**, *31*, 1900636.
- [14] X. Lan, Y. Cao, X. Liu, K. Xu, C. Liu, H. Zheng, K. Wang, *Adv. Intell. Syst.* **2021**, *3*, 2000182.
- [15] J. Zhou, T. Zhao, X. Shu, L. Liu, W. Lin, S. Chen, S. Shi, X. Yan, X. Liu, J. Chen, *Adv. Mater.* **2021**, *33*, 2103672.
- [16] W. Maass, T. Natschlagler, H. Markram, *Neural Comput.* **2002**, *14*, 2531.
- [17] H. Jaeger, H. Haas, *Science* **2004**, *304*, 78.
- [18] K. Nakajima, *Jpn. J. Appl. Phys.* **2020**, *59*, 060501.
- [19] K. Nakajima, I. Fischer, *Reservoir Computing Theory, Physical Implementations, and Applications*, Springer, Singapore, **2021**.
- [20] J. Torrejon, M. Riou, F. A. Araujo, S. Tsunegi, G. Khalsa, D. Querlioz, P. Bortolotti, V. Cros, K. Yakushiji, A. Fukushima, H. Kubota, S. Yuasa, M. D. Stiles, J. Grollier, *Nature* **2017**, *547*, 428.
- [21] T. Furuta, K. Fujii, K. Nakajima, S. Tsunegi, H. Kubota, Y. Suzuki, S. Miwa, *Phys. Rev. Appl.* **2018**, *10*, 034063.
- [22] S. Tsunegi, T. Taniguchi, S. Miwa, K. Nakajima, K. Yakushiji, A. Fukushima, S. Yuasa, H. Kubota, *Jpn. J. Appl. Phys.* **2018**, *57*, 120307.
- [23] S. Tsunegi, T. Taniguchi, K. Nakajima, S. Miwa, K. Yakushiji, A. Fukushima, S. Yuasa, H. Kubota, *Appl. Phys. Lett.* **2019**, *114*, 164101.
- [24] W. Jiang, L. Chen, K. Zhou, L. Li, Q. Fu, Y. Du, R. Liu, *Appl. Phys. Lett.* **2019**, *115*, 192403.
- [25] T. Kanao, H. Suto, K. Mizushima, H. Goto, T. Tanamoto, T. Nagasawa, *Phys. Rev. Appl.* **2019**, *12*, 024052.
- [26] D. Markovic, N. Leroux, M. Riou, F. Abreu Araujo, J. Torrejon, D. Querlioz, A. Fukushima, S. Yuasa, J. Trastoy, P. Bortolotti, J. Grollier, *Appl. Phys. Lett.* **2019**, *114*, 012409.
- [27] T. Yamaguchi, N. Akashi, S. Tsunegi, H. Kubota, K. Nakajima, T. Taniguchi, *Phys. Rev. Res.* **2020**, *2*, 023389.
- [28] T. Yamaguchi, N. Akashi, K. Nakajima, H. Kubota, S. Tsunegi, T. Taniguchi, *Sci. Rep.* **2020**, *10*, 19536.
- [29] N. Akashi, T. Yamaguchi, S. Tsunegi, T. Taniguchi, M. Nishida, R. Sakurai, Y. Wakao, K. Nakajima, *Phys. Rev. Res.* **2020**, *2*, 043303.
- [30] M. Riou, J. Torrejon, F. Abreu Araujo, S. Tsunegi, G. Khalsa, D. Querlioz, P. Bortolotti, N. Leroux, D. Markovic, V. Cros, K. Yakushiji, A. Fukushima, H. Kubota, S. Yuasa, M. D. Stiles, J. Grollier, *Reservoir Computing Leveraging The Transient Non-Linear Dynamics Of Spin-Torque NanoOscillators*, Springer, Singapore, **2021**, pp. 307–329.
- [31] T. Taniguchi, S. Tsunegi, S. Miwa, K. Fujii, H. Kubota, K. Nakajima, *Computing based on Spintronics Technology*, Springer Singapore, Singapore, **2021**, pp. 331–360.
- [32] F. Patten, S. Wolf, in *Proc. of Nonvolatile Memory Technology Conf.*, **1996**, pp. 1–2.
- [33] S. Gerardin, A. Paccagnella, *IEEE Trans. Nucl. Sci.* **2010**, *57*, 3016.
- [34] C. Hess, S. Metzger, *IAEA Bull.* **1985**, *27*, 16.
- [35] D. Lovering, *Scientific American* **2019**, <https://www.scientificamerican.com/article/three-mile-island-robots/> (accessed: September 2022).
- [36] U. Emi, S. Stapczynski, *The Japan Times* **2017**.
- [37] P. E. Dodd, L. W. Massengill, *IEEE Trans. Nucl. Sci.* **2003**, *50*, 583.
- [38] R. C. Baumann, *IEEE Trans. Dev. Mater. Reliab.* **2005**, *5*, 305.
- [39] Y. Conrau, J. Nozieres, V. Da Costa, M. Toulemonde, K. Ounadjela, *J. Appl. Phys.* **2003**, *93*, 7301.
- [40] R. R. Katti, J. Lintz, L. Sundstrom, T. Marques, S. Scoppettuolo, D. Martin, in *2009 IEEE Radiation Effects Data Workshop*, IEEE, Piscataway, NJ **2009**, pp. 103–105.
- [41] D. Kobayashi, Y. Kakehashi, K. Hirose, S. Onoda, T. Makino, T. Ohshima, S. Ikeda, M. Y. Manouchi, H. Sato, E. C. Enobio, T. Endoh, H. Ohno, *IEEE Trans. Nucl. Sci.* **2014**, *61*, 1710.
- [42] F. Ren, A. Jander, P. Dhagat, C. Nordman, *IEEE Trans. Nucl. Sci.* **2012**, *59*, 3034.
- [43] H. Hughes, K. Bussmann, P. J. McMarr, S. Cheng, R. Shull, A. P. Chen, S. Schafer, T. Mewes, A. Ong, E. Chen, M. H. Mendenhall, R. A. Reed, *IEEE Trans. Nucl. Sci.* **2012**, *59*, 3027.
- [44] D. Trivedi, C. D. Rahn, W. M. Kier, I. D. Walker, *Appl. Bionics Biomech.* **2008**, *5*, 99.
- [45] R. Sakurai, M. Nishida, H. Sakurai, Y. Wakao, N. Akashi, Y. Kuniyoshi, Y. Minami, K. Nakajima, in *2020 3rd IEEE Int. Conf. on Soft Robotics (RoboSoft)*, IEEE, Piscataway, NJ **2020** 710–717.
- [46] W. Sun, N. Akashi, Y. Kuniyoshi, K. Nakajima, in *2022 IEEE 5th Int. Conf. on Soft Robotics (RoboSoft)*, IEEE, Piscataway, NJ **2022**, pp. 409–415.

- [47] W. Sun, N. Akashi, Y. Kuniyoshi, K. Nakajima, *IEEE Rob. Autom. Lett.* **2022**, *7*, 6862.
- [48] Supporting information, which summarizes details of memory capacities and benchmark tasks.
- [49] J. C. Slonczewski, *J. Magn. Magn. Mater.* **1996**, *159*, L1.
- [50] S. S. Parkin, C. Kaiser, A. Panchula, P. M. Rice, B. Hughes, M. Samant, S.-H. Yang, *Nat. Mater.* **2004**, *3*, 862.
- [51] S. Yuasa, T. Nagahama, A. Fukushima, Y. Suzuki, K. Ando, *Nat. Mater.* **2004**, *3*, 868.
- [52] J. Williams, A. Difini Accioly, D. Rontani, M. Sciamanna, J.-V. Kim, *Appl. Phys. Lett.* **2019**, *114*, 232405.
- [53] T. Taniguchi, N. Akashi, H. Notsu, M. Kimura, H. Tsukahara, K. Nakajima, *Phys. Rev. B* **2019**, *100*, 174425.
- [54] Z. Yang, S. Zhang, Y. C. Li, *Phys. Rev. Lett.* **2007**, *99*, 134101.
- [55] A. Slavin, V. Tiberkevich, *IEEE Trans. Magn.* **2009**, *45*, 1875.
- [56] T. Yamaguchi, N. Akashi, K. Nakajima, S. Tsunegi, H. Kubota, T. Taniguchi, *Phys. Rev. B* **2019**, *100*, 224422.
- [57] A. Awad, P. Durrenfeld, A. Houshang, M. Dvornik, E. Iacocca, R. Dumas, J. Akerman, *Nat. Phys.* **2017**, *13*, 292.
- [58] M. Zahedinejad, H. Fulara, R. Khymyn, A. Houshang, M. Dvornik, S. Fukami, S. Kanai, H. Ohno, J. Akerman, *Nat. Mater.* **2022**, *21*, 81.
- [59] H. Kubota, K. Yakushiji, A. Fukushima, S. Tamaru, M. Konoto, T. Nozaki, S. Ishibashi, T. Saruya, S. Yuasa, T. Taniguchi, H. Arai, H. Imamura, *Appl. Phys. Express* **2013**, *6*, 103003.
- [60] T. Taniguchi, T. Ito, S. Tsunegi, H. Kubota, Y. Utsumi, *Phys. Rev. B* **2017**, *96*, 024406.
- [61] L. Appeltant, M. C. Soriano, G. Van der Sande, J. Danckaert, S. Massar, J. Dambre, B. Schrauwen, C. R. Mirasso, I. Fischer, *Nat. Commun.* **2011**, *2*, 468.
- [62] L. Larger, M. C. Soriano, D. Brunner, L. Appeltant, J. M. Gutierrez, L. Pesquera, C. R. Mirasso, I. Fischer, *Opt. Express* **2012**, *20*, 3241.
- [63] L. Larger, A. Baylon-Fuentes, R. Martinenghi, V. S. Udaltsov, Y. K. Chembo, M. Jacquot, *Phys. Rev. X* **2017**, *1*, 011015.
- [64] K. Fujii, K. Nakajima, *Phys. Rev. Appl.* **2017**, *8*, 024030.
- [65] K. Nakajima, K. Fujii, M. Negoro, K. Mitarai, M. Kitagawa, *Phys. Rev. Appl.* **2019**, *11*, 034021.
- [66] O. Rossler, *Phys. Lett. A* **1979**, *71*, 155.
- [67] I. Tsuda, *World Futures: J. Gen. Evol.* **1991**, *32*, 167.
- [68] D. M. Abrams, S. H. Strogatz, *Phys. Rev. Lett.* **2004**, *93*, 174102.
- [69] M. Zaks, A. Pikovsky, *Sci. Rep.* **2017**, *7*, 4648.
- [70] I. B. Yildiz, H. Jaeger, S. J. Kiebel, *Neural Networks* **2012**, *35*, 1.
- [71] L. M. Pecora, T. L. Carroll, *Phys. Rev. Lett.* **1990**, *64*, 821.
- [72] R. Toral, C. R. Mirasso, E. Hernandez-Garcia, O. Piro, *Chaos: Interdiscip. J. Nonlinear Sci.* **2001**, *11*, 665.
- [73] N. Bertschinger, T. Natschläger, *Neural Comput.* **2004**, *16*, 1413.
- [74] H. Jaeger, *GMD Technical Report*, German National Research Center for Information Technology, Bonn, Germany **2001**, p. 148.
- [75] J. Dambre, D. Verstraeten, B. Schrauwen, S. Massar, *Sci. Rep.* **2012**, *2*, 1.
- [76] M. A. M. Dzahir, S.-I. Yamamoto, *Robotics* **2014**, *3*, 120.
- [77] T. Kanno, D. Morisaki, R. Miyazaki, G. Endo, K. Kawashima, In *2015 IEEE Int. Conf. on Rehabilitation Robotics (ICORR)*, IEEE, Piscataway, NJ **2015**, pp. 565–570.
- [78] S. Koizumi, S. Kurumaya, H. Nabae, G. Endo, K. Suzumori, *IEEE Rob. Autom. Lett.* **2018**, *3*, 3240.
- [79] T. Abe, S. Koizumi, H. Nabae, G. Endo, K. Suzumori, N. Sato, M. Adachi, F. Takamizawa, *IEEE Rob. Autom. Lett.* **2019**, *4*, 2532.
- [80] T. Miyazaki, T. Tagami, D. Morisaki, R. Miyazaki, T. Kawase, T. Kanno, K. Kawashima, *Appl. Sci.* **2019**, *9*, 2869.
- [81] W. Parkinson, O. Sisman, *Nucl. Eng. Des.* **1971**, *17*, 247.
- [82] O. D. Yirmibeşoğlu, T. Oshiro, G. Olson, C. Palmer, Y. Menguç, *Front. Rob. AI* **2019**, *6* 40.
- [83] T. Tagami, T. Kawase, D. Morisaki, R. Miyazaki, T. Miyazaki, T. Kanno, K. Kawashima, in *2018 IEEE/RSJ Int. Conf. on Intelligent Robots and Systems (IROS)*, IEEE, Piscataway, NJ **2018**, p. 27622767.
- [84] G.-B. Huang, Q.-Y. Zhu, C.-K. Siew, *Neurocomputing* **2006**, *70*, 489.
- [85] X. Chen, F. A. Araujo, M. Riou, J. Torrejon, D. Ravelosona, W. Kang, W. Zhao, J. Grollier, D. Querlioz, *Nat. Commun.* **2022**, *13*, 1016.
- [86] D. Kobayashi, K. Hirose, T. Makino, S. Onoda, T. Ohshima, S. Ikeda, H. Sato, E. C. I. Enobio, T. Endoh, H. Ohno, *Jpn. J. Appl. Phys.* **2017**, *56*, 0802B4.
- [87] M. S. Kulkarni, C. Teuscher, In *2012 IEEE/ACM Int. Symp. on Nanoscale Architectures (NANOARCH)*, IEEE, Piscataway, NJ **2012**, pp. 226–232.
- [88] C. Du, F. Cai, M. A. Zidan, W. Ma, S. H. Lee, W. D. Lu, *Nat. Commun.* **2017**, *8*, 2204.
- [89] A. Z. Stieg, A. V. Avizienis, H. O. Sillin, C. Martin-Olmos, M. Aono, J. K. Gimzewski, *Adv. Mater.* **2012**, *24*, 286.
- [90] H. O. Sillin, R. Aguilera, H.-H. Shieh, A. V. Avizienis, M. Aono, A. Z. Stieg, J. K. Gimzewski, *Nanotechnology* **2013**, *24*, 384004.
- [91] E. C. Demis, R. Aguilera, H. O. Sillin, K. Scharnhorst, E. J. Sandouk, M. Aono, A. Z. Stieg, J. K. Gimzewski, *Nanotechnology* **2015**, *26*, 204003.
- [92] D. Brunner, M. C. Soriano, C. R. Mirasso, I. Fischer, *Nat. Commun.* **2013**, *4*, 1364.
- [93] K. Vandoorne, P. Mechet, T. Van Vaerenbergh, M. Fiers, G. Morthier, D. Verstraeten, B. Schrauwen, J. Dambre, P. Bienstman, *Nat. Commun.* **2014**, *5*, 3541.
- [94] S. Ghosh, T. Paterek, T. C. Liew, *Phys. Rev. Lett.* **2019**, *123*, 260404.
- [95] D. Sussillo, L. F. Abbott, *Neuron* **2009**, *63*, 544.
- [96] R. Laje, D. V. Buonomano, *Nature Neurosci.* **2013**, *16*, 925.
- [97] K. Inoue, K. Nakajima, Y. Kuniyoshi, *Sci. Adv.* **2020**, *6*, eabb3989.